



Research paper

In-situ C-N-S-tridoped single crystal black TiO₂ nanosheets with exposed {001} facets as efficient visible-light-driven photocatalysts

Xu Yan^a, Zipeng Xing^{a,*}, Yan Cao^a, Mengqiao Hu^a, Zhenzi Li^b, Xiaoyan Wu^b, Qi Zhu^a, Shilin Yang^{a,*}, Wei Zhou^{a,*}

^a Department of Environmental Science, School of Chemistry and Materials Science, Key Laboratory of Functional Inorganic Material Chemistry, Ministry of Education of the People's Republic of China, Heilongjiang University, Harbin 150080, PR China

^b Department of Epidemiology and Biostatistics, Harbin Medical University, Harbin 150086, PR China

ARTICLE INFO

Article history:

Received 4 April 2017

Received in revised form 14 July 2017

Accepted 1 August 2017

Available online 2 August 2017

Keywords:

Single crystal TiO₂

C-N-S-tridoping

Nanosheet

{001} facet

Visible-light-driven photocatalysis

ABSTRACT

In-situ C-N-S-tridoped single crystal black TiO₂ nanosheets with exposed {001} facets are successfully fabricated via a facile hydrothermal method combined with an in-situ solid-state chemical reduction approach, followed by calcination at 450 °C. The crystal structure, crystallinity, morphology and composition of the as-prepared samples are investigated through X-ray diffraction, Raman, scanning electron microscopy, transmission electron microscopy, X-ray photoelectron spectroscopy, and UV-vis diffuse reflectance spectroscopy, respectively. The results suggest that the obtained C-N-S-tridoped single crystal black TiO₂ nanosheets exhibit uniform nanosheet-like structure with exposed {001} facets and average length of ~300–400 nm, thickness of ~20 nm. The visible-light photocatalytic degradation rate of methyl orange is up to 92.13%, and photocatalytic hydrogen evolution is 149.7 μmol h⁻¹ g⁻¹. The excellent photocatalytic activity can be ascribed to the synergistic effect of surface heterojunction between {001} and {101} facets, the C-N-S-tridoping, and the formed Ti³⁺ species in photocatalyst, which can not only favor the visible-light absorption but also facilitate the separation and transfer of photogenerated charges.

© 2017 Elsevier B.V. All rights reserved.

1. Introduction

With the increasing environment issue and energy crisis, eliminating environmental pollutants and hydrogen production from water splitting via semiconductor photocatalysis has become a promising approach [1]. Among various active photocatalyst materials, titanium dioxide (TiO₂) has received a lot of attention for pollutant degradation [2], photocatalytic hydrogen evolution [3], dye-sensitized solar cells [4], and other photocatalytic applications [5] owing to its nontoxicity, superior photocatalytic activity, good stability, and low cost [6–8]. However, the widespread application of pure TiO₂ is greatly restrained by two major barriers. Firstly, the wide band gap (~3.2 eV for anatase) restricts its photocatalytic activity in the visible region. Secondly, the fast recombination of photogenerated electron-hole pairs results in low efficiency of photoinduced chemical reactions [9,10]. Thus numerous approaches have been proposed to narrow the band gap and restrain the photogenerated electron-hole pair recombination. To date, the highly

active TiO₂ can be prepared by various methods such as metal and non-metal elements doping [11], surface sensitization [12], and so on [13]. Doping TiO₂ with metal or nonmetal elements is an intelligent strategy to narrow the band gap and decrease the required activation energy [14]. In fact, nonmetal doping is thought to be more effective and environmentally-friendly than metal doping which has lower thermal stability and the decreased electron-hole recombination sites [15,16]. N-Doped TiO₂ can significantly improve the visible light absorption properties through embedding N atom into the lattice of TiO₂, which can create a hybrid orbital (the overlap of oxygen 2p states and nitrogen 2p states) above the valence band (VB) of TiO₂, thus showing an enhanced visible light photocatalytic performance [17,18]. S-doped TiO₂ reveals the improvement due to narrowing of the band gap through the overlap of sulfur 3p states and oxygen 2p states and thus expands the photoresponse to the visible light region [19]. Moreover, C-doped TiO₂ achieves the same purpose because a hybrid orbit can be formed above the VB of TiO₂ by replacing lattice Ti atom or lattice O atom into carbon atoms [20,21]. Therefore, it may be still a challenge to dope TiO₂ with three kinds of nonmetal elements simultaneously to improve the photocatalytic activity owing to the merits benefited from each dopant [22,23].

* Corresponding authors.

E-mail addresses: xingzipeng@hlju.edu.cn (Z. Xing), ysl3000@126.com (S. Yang), zwchem@hotmail.com (W. Zhou).

Anatase TiO_2 single crystal nanosheet with highly energetic {001} facet has attracted great interest because of its fascinating shape-dependent physicochemical properties [24,25]. A surface heterojunction concept based on the density functional theory (DFT) calculation explains the enhanced photocatalytic activity of TiO_2 as a result of photoinduced electrons and holes migrate to {101} and {001} facets, respectively [26,27]. Therefore, it is believed that TiO_2 nanosheets doped with C, N and S atoms to form C-N-S- TiO_2 nanosheets will be a photocatalyst with superior photocatalytic activity. In addition to controlling the exposed plane, engineering defects on the TiO_2 nanosheet is another advancing way to enhance the utilization of solar energy [28,29]. Mao et al. [30] prepared black TiO_2 nanomaterials through the hydrogenation of TiO_2 , showing excellent photocatalytic activity under visible light irradiation. Since then, numerous methods have been devoted to the synthesis of black TiO_2 materials, including hydrogenation [31], high pressure [32], plasma assisted hydrogenation [33], chemical reduction [34], and so on [35]. It is found that introducing the disordered surface layers, Ti^{3+} , and oxygen vacancy (O_v) on the surface of TiO_2 can not only shift optical absorption from the ultraviolet to near-infrared regions but also lead to a superior ability of photocatalytic degradation of pollutants and H_2 evolution from H_2O [36–38]. Therefore, the exploitation of photocatalytic system with high performance black TiO_2 -based materials is promising.

Herein, in this paper, in-situ C-N-S-tridoped single crystal black TiO_2 nanosheets with exposed {001} facets are fabricated for the first time through a hydrothermal method and an in-situ controllable solid-state reaction strategy. To the best of our knowledge, there is still lack of information about a systematic research of C-N-S-tridoped black TiO_2 -based nanosheets. The prepared photocatalyst with exposed {001} facets and narrow band gap exhibits excellent photocatalytic activity for methyl orange removal and hydrogen evolution under visible-light irradiation. Moreover, the photocatalytic mechanism of the as-prepared C-N-S-tridoped single crystal black TiO_2 nanosheets is also investigated.

2. Materials and methods

2.1. Materials

Tetrabutyl titanate (TBOT), absolute ethanol (EtOH), 40% hydrofluoric acid (HF, 40%), glacial acetic acid (HAc, 99.5%), and cystine were purchased from Tianjin Kermel Chemical Reagent Co. Ltd, China. Sodium boron hydride (NaBH_4 , 98%) was purchased from Aladdin Reagent Company, China. All of the chemicals used in this work were analytical grade and employed without further purification. Deionized (DI) water was used throughout this study.

2.2. Synthesis of C-N-S-tridoped single crystal black TiO_2 nanosheets

The C-N-S-tridoped single crystal TiO_2 nanosheets were prepared by one-step hydrothermal method. In detail, 1.95 mL of deionized water, 0.3 mL of 40 wt% HF, and 28.6 mL of HAc were mixed together to form a clear solution in a Teflon cup. Then, 1.7 mL of TBOT was added dropwise to solution with continuous stirring. Afterwards, 0.5 g of cystine was added to the reaction solution. After the 30 min of magnetic stirring, the mixture was transferred into a 50 mL Teflon-lined stainless steel autoclave, which was heated at 180 °C for 24 h. After hydrothermal reaction, the obtained brown powders were collected and washed with distilled water and ethanol for three times, and dried overnight at 60 °C. Finally, the as-prepared samples were calcinated at 450 °C in air for 2 h. It denoted as C-N-S- TiO_2 . For comparsion, the TiO_2 nanosheets were also synthesized under the same condition without cystine. Then,

the C-N-S-tridoped single crystal black TiO_2 nanosheets were prepared by in-situ controllable solid-state reaction strategy (Fig. 1). Typically, the 2 g of the prepared C-N-S-tridoped TiO_2 powders were mixed with 4 g of NaBH_4 at room temperature for 30 min thoroughly. The mixtures were transferred into porcelain boats, and placed in a tubular furnace, deaerated under inert gas flow (Ar) for 0.5 h, subsequently, heated to 350 °C for 2 h under Ar atmosphere at a heating rate of 6 °C min⁻¹ and then annealed for 1 h at 350 °C. After naturally cooling down to room temperature, the black C-N-S- TiO_2 nanosheets were obtained and simply washed with deionized water for three times to get rid of unreacted NaBH_4 , and dried at 60 °C. It denoted as b-C-N-S- TiO_2 .

2.3. Characterization

The crystal structures of the samples were confirmed by an X-ray diffraction (XRD-D8 Advance, Bruker), using Cu K α radiation ($\lambda = 1.5406 \text{ \AA}$), operating at 40 kV and 50 mA. The Raman spectra were recorded in a Jobin Yvon HR 800 micro-Raman spectrometer with a 457.9 nm laser. The morphology was characterized by a field emission scanning electron microscope (FE-SEM, Hitachi S-4800) and a transmission electron microscope (TEM JEOL JEM-2010) with an accelerating voltage of 200 kV. X-ray photoelectron spectroscopy (XPS) was done on a Kratos- ULTRA AXIS DLD system with Al K α X-ray source. All the binding energies were referenced to the surface adventitious carbon of 284.6 eV. The UV-vis diffuse reflectance spectra (DRS) were obtained using a TU-1901 spectrophotometer. BaSO_4 was used as the background ranging from 190 to 800 nm in a UV-vis diffuse reflectance study. The electrochemical impedance spectroscopy (EIS) was recorded by a computer-controlled IM6e Impedance measurement unit (Zahner Elektrik, Germany).

2.4. Photocatalytic degradation

To examine the photocatalytic activities of as-prepared samples, the photocatalytic degradation for methyl orange (MO) were carried out under visible light irradiation with a 300 W Xeon-lamp equipped with a 420 nm cut-off filter. The photocatalytic reaction was processing in a Pyrex glass vessel, and 50 mg of photocatalysts were added into 50 mL of 10 mg L⁻¹ MO aqueous solution. Before irradiation, the suspension was magnetically stirred in dark for 30 min to keep an adsorption-desorption equilibrium. After 180 min photocatalytic reaction, the reaction solution was immediately centrifuged and filtrated. Finally, the supernatants were analyzed at $\lambda = 464 \text{ nm}$ by a T6 UV-vis spectrophotometer for calculating the concentration of MO.

2.5. Photocatalytic hydrogen evolution

The photocatalytic H_2 -production experiments were carried out in an online photocatalytic hydrogen generation system (AuLight, Beijing, CEL-SPH2N) at room temperature. An AM 1.5 solar power system (solar simulator (Oriel, USA) with an AM 1.5G filter (Oriel, USA)) was used as the light source. In a typical H_2 -generated experiment, 50 mg of catalysts were added into a 100 mL of aqueous solution (containing 20 mL of methanol) used as the sacrificial reagent in closed-gas circulation reaction cell. Prior to irradiation, the suspension was bubbled with N_2 several times to completely remove the dissolved oxygen. The produced hydrogen was periodically analyzed by an on-line gas chromatography (SP7800, TCD, molecular sieve 5 Å, N_2 carrier, Beijing Keruida, Ltd) with the interval of each 1 h.

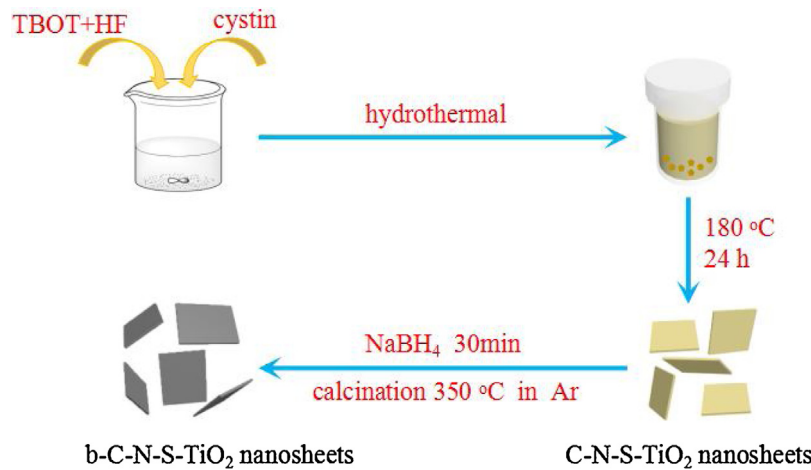


Fig. 1. Schematic diagram for the formation of single crystal black C-N-S-TiO₂ nanosheets.

3. Results and discussion

The crystallinity and crystal phase of the prepared samples may greatly influence the photocatalytic performance and largely determine its suitability for practical applications [39,40]. Therefore, X-ray diffraction (XRD) patterns are carried out to analyze the phase structures and crystallinity of the prepared TiO₂ samples. As shown in Fig. 2a, the diffraction peaks can be well-indexed for anatase TiO₂ phase (JCPDS #21-1272). No other impurity peak is detected in the C-N-S-TiO₂. Nevertheless, the C-N-S-TiO₂ exhibits a relatively small variation on anatase peak compared with the pristine TiO₂ nanosheets, indicating the insignificant change of phase structures in tridoped TiO₂ samples, which is mostly due to the low doping percentage. As calculated from the (101) Bragg diffraction using the Scherrer equation, C-N-S-TiO₂ possesses larger average crystallite sizes of 28.2 nm than that of pristine TiO₂ (24.5 nm). The lattice parameters (a, b, and c) for C-N-S-TiO₂ and pristine TiO₂ are 3.782, 3.782, and 9.535, and 3.784, 3.784, and 9.537 Å, respectively, indicating that the tridope treatment leads to the distortion of the structures in C-N-S-TiO₂ even though it does not change the anatase phase [41,42]. Compared with TiO₂ and C-N-S-TiO₂, the intensity of b-TiO₂ and b-C-N-S-TiO₂ diffraction peaks are evidently decreased and broadened, the change of crystalline structure may be related to the effect of oxygen vacancies (O_v) and the presence of Ti³⁺, leading to the disorder-induced lattice and slightly reduced crystallite size [43].

To further study the phase compositions of tridoped TiO₂ samples, the Raman spectra of TiO₂, b-TiO₂, C-N-S-TiO₂, and

b-C-N-S-TiO₂, respectively, are illustrated in Fig. 2b. For as-prepared samples, the characteristic Raman peaks exhibit six ($3E_g + 2B_{1g} + A_{1g}$) Raman-active modes, five characteristic Raman peaks locate at around 144, 197, 397, 516 and 639 cm⁻¹ reveal that the dominate phase is the anatase TiO₂ [44]. Notably, compared with pristine TiO₂ nanosheets, a slightly blue shift at 160 cm⁻¹, which can be observed for tridoped TiO₂ samples, indicating that some O atoms in the lattice of TiO₂ have been replaced by C, N and S atom [45]. Moreover, following by treatment with NaBH₄, the E_g¹ peaks of b-TiO₂ and b-C-N-S-TiO₂ show a further blue shift. As reported in the previous studies, the Ti³⁺ and oxygen deficiency are formed in TiO₂ lattice as a result of the reduction of NaBH₄ [46]. Obviously, the Raman results are correlating well with the XRD characterization.

The morphology and microstructure of b-C-N-S-TiO₂ are characterized by SEM and TEM. TiO₂ nanosheets still keep the pristine morphology and microstructure after the NaBH₄ treatment process. As observed from SEM image of Fig. 3a, it exhibits uniform nanosheet-like structure. Noticeably, when compared with the pristine TiO₂ nanosheets, the morphology of the tridoped TiO₂ samples is nearly unchanged, which may be due to a little amount of C, N and S incorporating into the TiO₂ lattice during hydrothermal procedure [47]. It could be found from Fig. 3b that the nanosheets possess average length of ~300–400 nm, thickness of ~20 nm and appear smooth surface. In addition, the inset of Fig. 3b clearly shows the selected area electron diffraction (SAED) pattern, indicating that the as-prepared samples are well-developed single crystal. Moreover, the energy-dispersive X-ray spectrometry (EDX) reveals

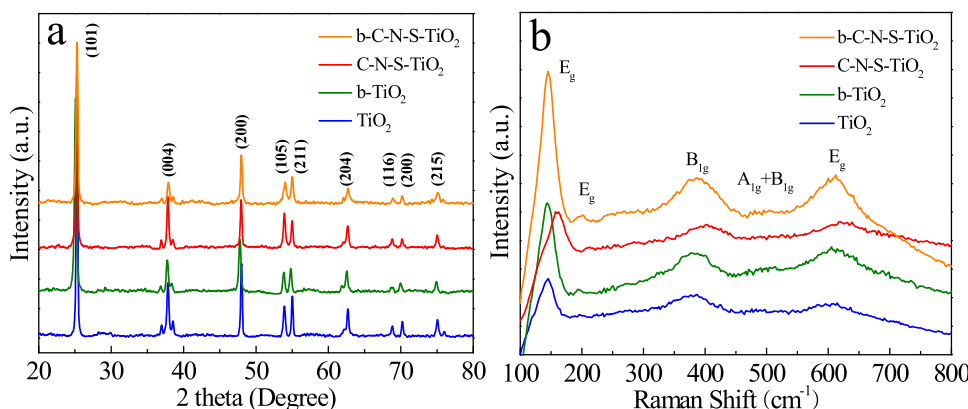


Fig. 2. XRD patterns (a) and Raman spectra (b) of TiO₂, b-TiO₂, C-N-S-TiO₂, and b-C-N-S-TiO₂, respectively.

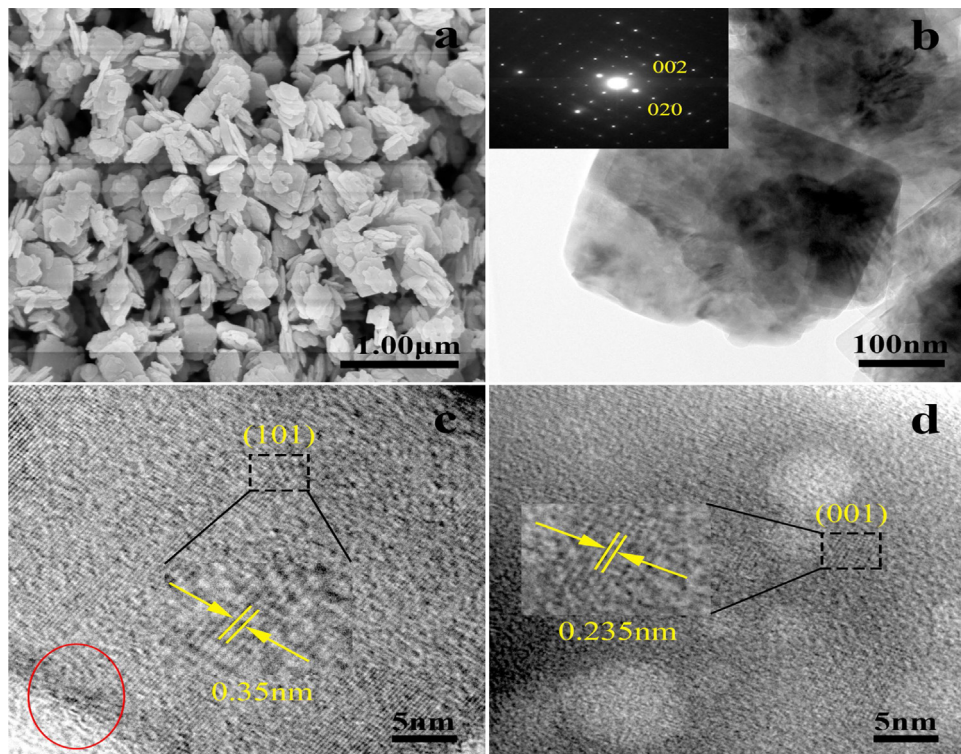


Fig. 3. SEM (a), TEM (b), and HRTEM images (c and d) of b-C-N-S-TiO₂. The inset of (b) is the corresponding SAED pattern.

the existence of Ti, O, C, N and S elements in the b-C-N-S-TiO₂ samples (Fig. S2). Fig. 3c and d displays the HRTEM images of the b-C-N-S-TiO₂ materials, the lattice fringe spacing of 0.35 nm and 0.235 nm are corresponding to the {101} and {001} planes of anatase TiO₂, respectively [28,48]. Notably, the thin surface disordered shell which are marked in Fig. 3c by the red line can be obviously observed, indicating that the efficient modification of the b-C-N-S-TiO₂ materials by NaBH₄ treatment [49].

In order to investigate the chemical state of element and surface chemical composition, the b-C-N-S-TiO₂ sample is analyzed by X-ray photoelectron spectroscopy (XPS), and the XPS analysis of Ti 2p, O 1s, C 1s, N 1s, and S 2p are shown in Fig. 4. The XPS full spectrum is shown in Fig. 4a, which indicates the existence of Ti, O, C, N and S elements. The Ti 2p XPS spectra of the b-C-N-S-TiO₂ displays in Fig. 4b, the peak located at 463.7, 461.7, 458.5 and 457.4 eV are assigned to Ti⁴⁺ 2p_{1/2}, Ti³⁺ 2p_{1/2}, Ti⁴⁺ 2p_{3/2}, and Ti³⁺ 2p_{3/2}, respectively. These Ti³⁺ species are created due to the Ti⁴⁺ reduction of TiO₂ with the treatment of NaBH₄ [50]. Meanwhile, the corresponding high-resolution XPS spectrum of O 1s region is shown in Fig. 4c. The O 1s peak can be fitted into two peaks with characteristic binding energies of 529.5 and 531.0 eV, implying the formation of two different types of O 1s states. These peaks are attributed to lattice oxygen (Ti—O) and hydroxyl groups —OH, which is further demonstrated by the fact that Ti³⁺ and O_v are successfully formed thereby narrow the band gap and inhibit the combination of photogenerated electron–hole pairs [51]. As displayed in Fig. 4d, three peaks are observed in the XPS spectrum of C 1s for b-C-N-S-TiO₂ at 284.6, 286.1 and 288.6 eV, respectively. The peak at 284.6 eV is assigned to hydrocarbons which because of organic precursor and adventitious carbon, while the signal at the binding energy of 286.1 and 288.6 eV indicate C—O bond and C=O bond, respectively. The peak at 288.6 eV can be attributed to the substitution of Ti atom by C and the formation of Ti—O—C [52,53]. Fig. 4e shows the XPS of b-C-N-S-TiO₂ in the N 1s binding energy regions. On the one hand, the main peak at binding energy of 399.7 eV can be attributed to

the presence of substitutional nitrogen state as the characteristic of O—Ti—N arising from the partly lattice oxygen is substituted by N atom. On the other hand, a small peak at 400.9 eV is observed due to the existence of interstitial nitrogen atoms as Ti—O—N in the as-prepared samples [54,55]. Therefore, those results indicate that N atom has been doped into TiO₂ nanosheets successfully. Fig. 4f displays the S 2p peak with characteristic binding energies of 168.3 eV. Peak at 168.3 eV can be assigned to the S⁶⁺ species, corresponding to the substitution of Ti⁴⁺ by S⁶⁺, which is much easier than the replacement of O²⁻ with S²⁻ [56]. Besides, the amount of elements doped are also confirmed by XPS and the mass concentration of C, N and S are 14.20, 4.80 and 3.30%, respectively (Table S1).

UV-vis diffuse reflectance spectrum is used to evaluate the light absorption and band gap of the as-prepared samples. It is clearly shown in Fig. 5a that the pristine TiO₂ nanosheets with a wide band gap mainly exhibit strong absorption in the ultraviolet region, while the b-TiO₂ nanosheets can absorb both UV and visible light. Notably, the visible absorption of the C-N-S-tridoped TiO₂ powders is significantly enhanced after doping with C, N and S. The enhanced visible light absorption is attributed to the tridoping narrowing the band gap of TiO₂ [57]. In addition, compared to C-N-S-TiO₂, the absorption of b-C-N-S-TiO₂ exhibits a red-shift to visible light region, which is probably caused by the formation of Ti³⁺ species and O_v [58]. It has been reported that Ti³⁺ and O_v can break the selection rule for indirect transitions of TiO₂ and improve absorption for photon energy [59]. Moreover, an enhanced absorption in visible light region is consistent with the dark color of the b-C-N-S-TiO₂, the color of b-C-N-S-TiO₂ after six months still keep black, indicating the excellent stability of the black TiO₂ (Fig. S1). Fig. 5b shows the indirect band gaps of all the samples. The band gaps of TiO₂, b-TiO₂, C-N-S-TiO₂ and b-C-N-S-TiO₂ are 3.07, 2.66, 2.95 and 2.51 eV, respectively. Consequently, the formation of Ti³⁺ and O_v with the treatment of NaBH₄ as well as chemical bonding through tridoping with C, N and S are beneficial to improve the visible light

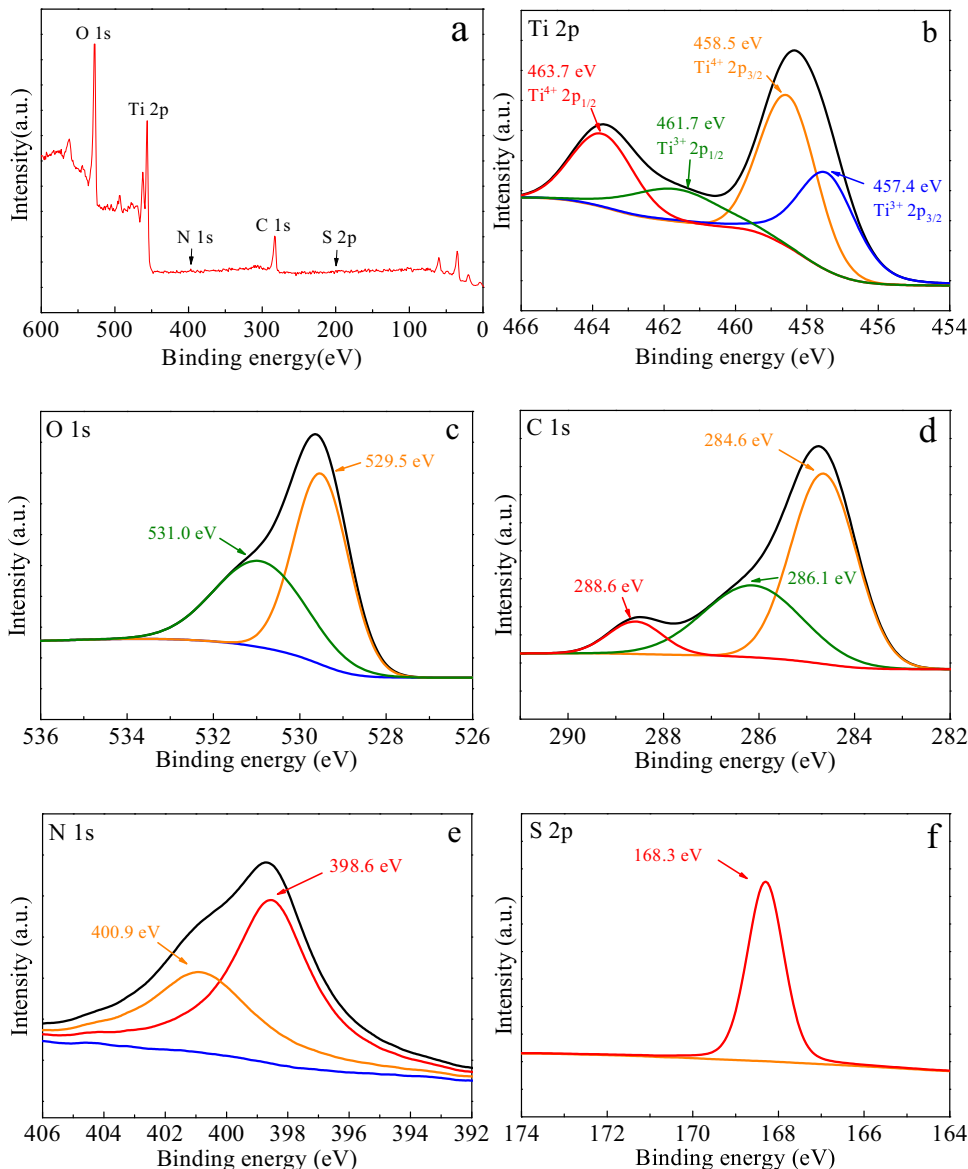


Fig. 4. The full-scale XPS spectrum (a), Ti 2p (b), O 1s (c), C 1s (d), N 1s (e), and S 2p (f) of b-C-N-S-TiO₂.

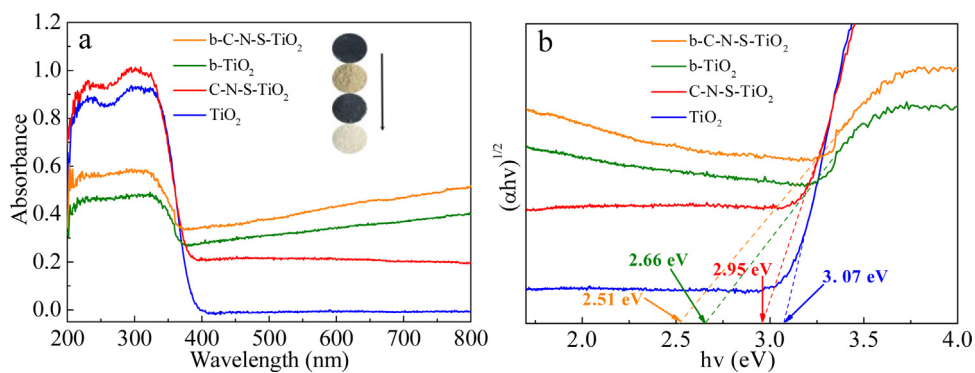


Fig. 5. UV-vis diffuse reflectance absorption spectra (a) and determination of the indirect interband transition energies (b) for TiO₂, b-TiO₂, C-N-S-TiO₂, and b-C-N-S-TiO₂, respectively.

absorption properties, which favors the visible-light-driven photocatalytic performance as discussed below.

Fig. 6a and **b** shows the degradation rate and the reaction kinetic curves of different samples by MO degradation under visible-light

irradiation. The blank test is proved that the degradation of MO is negligible under visible light irradiation without catalysts. As is shown in **Fig. 6a**, in comparison to the pristine TiO₂ nanosheets with the MO removal of about 42.38% within 180 min, the degradation

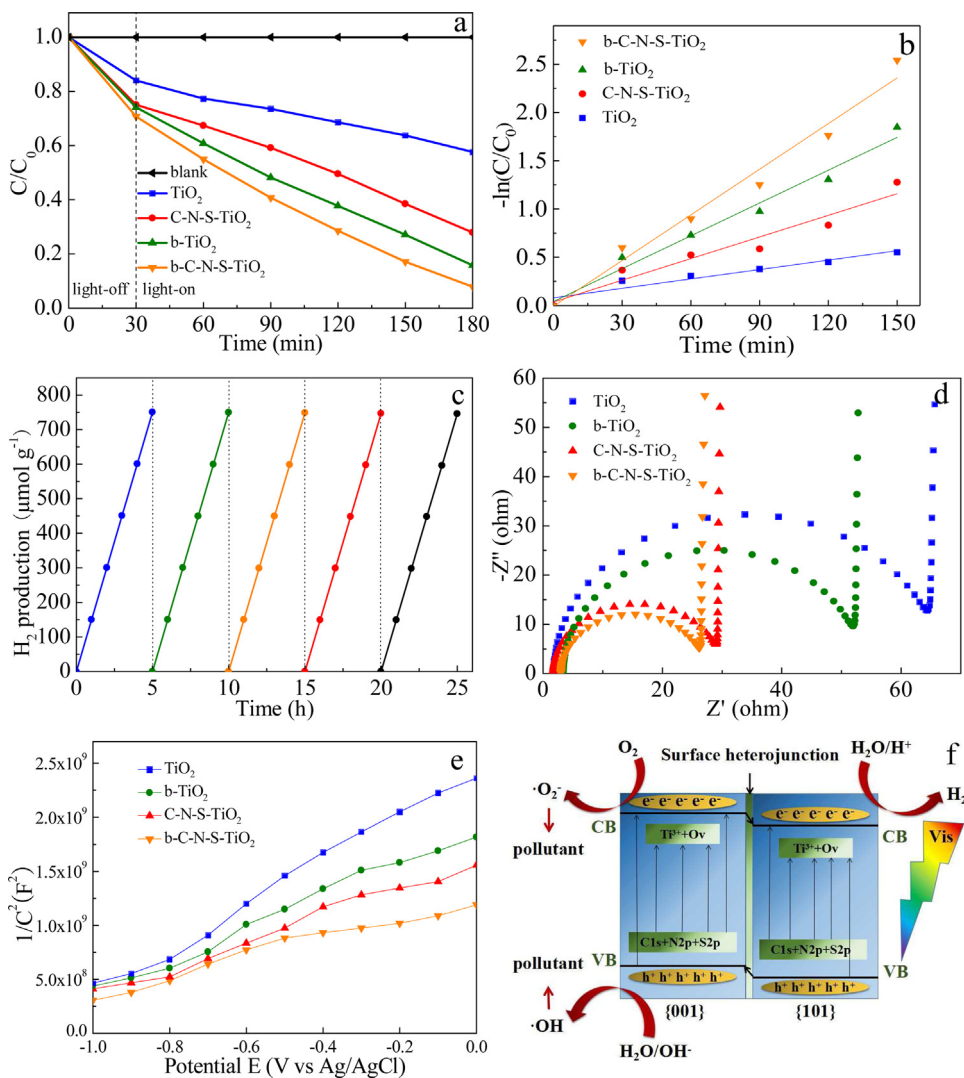


Fig. 6. (a) Photocatalytic MO degradation rate by using different samples under visible-light irradiation, (b) variations of $-\ln(C/C_0)$ versus visible-light irradiation time with different samples, (c) the recyclability of b-C-N-S-TiO₂ during the photocatalytic H₂ evolution under AM 1.5 irradiation, (d) Electrochemical impedance spectra, (e) the Mott-Schottky plots of TiO_2 , b-TiO_2 , C-N-S-TiO_2 , and b-C-N-S-TiO₂, respectively, and (f) Schematic illustration of the visible-light-driven photocatalytic mechanism for black C-N-S-TiO₂ nanosheet photocatalyst.

efficiency of b-TiO₂ and C-N-S-TiO₂ are 84.22 and 72.12%, respectively. As expected, the b-C-N-S-TiO₂ exhibits the unbelievable photocatalytic activity under visible light irradiation, which can be up to 92.13%. The increased degradation rate may be assigned to following aspects: (a) introducing Ti³⁺ of C-N-S-TiO₂ can promote the separation of photogenerated charge carriers and accelerate the electron transfer, (b) doping with C, N and S can highly narrow the band gap of TiO₂ nanosheets and improve the visible light absorption. Meanwhile, the corresponding first-order reaction rate constants (k) are calculated and revealed in Fig. 6b. The k values of TiO_2 , b-TiO₂, C-N-S-TiO₂ and b-C-N-S-TiO₂ are 0.0032, 0.0113, 0.0075 and 0.0158 min^{-1} , respectively. It is exciting that the k value of b-C-N-S-TiO₂ is about 5 times higher than that of pristine TiO₂ nanosheets.

The photocatalytic hydrogen evolution activities are tested through the photocatalytic water splitting process under the solar light (AM 1.5) irradiation. The pristine TiO₂ nanosheets show low photocatalytic hydrogen generation activity due to the high recombination of photoinduced electron-hole pairs. In particular, the highest hydrogen evolution rate, obtained for b-C-N-S-TiO₂, is $149.7 \mu\text{mol h}^{-1} \text{ g}^{-1}$. This value exceeds to b-TiO₂ and C-N-S-TiO₂. It indicates that the C, N and S tri-doped, the introduction of Ti³⁺ and

the heterojunction between {001} and {101} facets all contribute to improve the photocatalytic activity. The recycling hydrogen evolution reaction is conducted to detect the photocatalyst stability of b-C-N-S-TiO₂ and the results are shown in Fig. 6c. The hydrogen evolution rates after five cycles lasting 25 h still keep constant, indicating the high stability of b-C-N-S-TiO₂ photocatalyst.

Moreover, electrochemical impedance spectrum (EIS) is used to investigate the separation efficiency of the photoexcited charge carriers. A smaller impedance arc radius on the EIS Nyquist plot indicates a smaller electric resistance of the electrode. Fig. 6d shows the Nyquist curves of TiO_2 , b-TiO₂, C-N-S-TiO₂ and b-C-N-S-TiO₂ photocatalyst. It can be clearly seen that impedance arc radius for the b-C-N-S-TiO₂ is much smaller than that of others. Similarly, photocatalytic activity of b-TiO₂ is stronger than that of pristine TiO₂ nanosheets. This implies that the synergistic effect of the b-C-N-S-TiO₂ nanosheets leads to a faster and effective electron-hole transfer by inhibiting the recombination of electron-hole pairs.

As shown in Fig. 6e, the Mott-Schottky (M-T) plots for the resultant samples exhibit the typical n-type semiconductor with the positive slopes. The b-C-N-S-TiO₂ nanosheets show the smaller slope than that of TiO_2 , b-TiO₂, and C-N-S-TiO₂, indicating a higher charge carrier density due to the presence of Ti³⁺, C, N, and S in the

single crystal TiO_2 nanosheets, which may be responsible for the enhance photocatalytic and photoelectrochemical performances.

On the basis of the above systematic analysis, a possible mechanism explaining the enhanced photocatalytic activity of b-C-N-S-TiO₂ photocatalyst is proposed and shown in Fig. 6f. When the black C-N-S-TiO₂ nanosheets are irradiated by visible light, the VB electrons of TiO₂ are excited to the CB, while the holes remain in VB. Because of the formation of surface heterojunction, the photogenerated electrons and holes transfer to {101} and {001} facets, respectively, which can effectively inhibit the recombination of electrons-holes [24,28]. Furthermore, after addition of cystine, C, N and S species are tri-doped into the lattice of TiO₂ nanosheets. The doped C, N and S elements can generate additional impurity level above the VB of TiO₂ nanosheet [19,20,41]. What's more, the introduction of Ti³⁺ and O_v can create an additional band below the CB of TiO₂, which synergistically narrow the band gap of TiO₂ nanosheets and further improve the visible light absorption [29,31]. Therefore, the photogenerated holes can easily react with the water or hydroxide ions (OH⁻) to form hydroxyl radicals (-OH), and the photogenerated electrons can capture the dissolved oxygen to generate the superoxide anion radicals (•O²⁻). Eventually, the organic pollutants are completely mineralized by active species (•OH and •O²⁻). The excited electrons in the CB on the surface can split water to produce H₂.

4. Conclusions

In summary, we demonstrated an in-situ fabrication of visible light active b-C-N-S-TiO₂ single crystal nanosheets photocatalyst through a facile hydrothermal process combined with an in-situ controllable solid state reaction method. The obtained photocatalyst exhibited uniform nanosheet-like structure and C, N, S were doped into the TiO₂ nanosheets successfully. Compared with pristine TiO₂ nanosheets, black TiO₂ nanosheets and C-N-S-tridoped TiO₂ nanosheets, the optimum photocatalytic activity of the b-C-N-S-TiO₂ nanosheets towards the degradation of MO and evolution of H₂ were obtained. The excellent photocatalytic performance of b-C-N-S-TiO₂ nanosheets were attributed to the synergistic effect of surface heterojunction between {001} and {101} facets, the tridoping with C, N and S, and the formed Ti³⁺ species in photocatalyst, which contributed to narrow the band gap and promote the separation and transfer of photogenerated charge carriers. Therefore, the novel doped TiO₂ photocatalyst may provide new insights for wastewater treatment and hydrogen evolution in practical applications.

Acknowledgments

We gratefully acknowledge the support of this research by the National Natural Science Foundation of China (21376065, 51672073 and 81573134), the Heilongjiang Postdoctoral Startup Fund (LBH-Q14135), the China Postdoctoral Science Foundation (2017M611399), the Postdoctoral Science Foundation of Heilongjiang Province (LBH-Z16150), the University Nursing Program for Young Scholars with Creative Talents in Heilongjiang Province (UNPYSCT-2015014, UNPYSCT-2016018), the Innovative Science Research Project of Harbin Medical University (2016JCZX13), and the Postgraduate Innovative Science Research Project of Heilongjiang University (YJSCX2017-163HLJU).

Appendix A. Supplementary data

Supplementary data associated with this article can be found, in the online version, at <http://dx.doi.org/10.1016/j.apcatb.2017.08.005>.

References

- [1] W. Ong, L. Tan, S. Chai, S. Yonga, A.R. Mohamed, *Nanoscale* 6 (2014) 1946–2008.
- [2] Z. Xing, W. Zhou, F. Du, Y. Qu, G. Tian, K. Pan, C. Tian, H. Fu, *Dalton Trans.* 43 (2014) 790–798.
- [3] L. Zhang, Z. Xing, H. Zhang, Z. Li, X. Wu, X. Zhang, Y. Zhang, W. Zhou, *Appl. Catal. B* 180 (2016) 521–529.
- [4] W. Wang, M.O. Tadé, Z. Shao, *Chem. Soc. Rev.* 44 (2015) 5371–5408.
- [5] W. Zhou, W. Li, J. Wang, Y. Qu, Y. Yang, Y. Xie, K. Zhang, L. Wang, H. Fu, D. Zhao, *J. Am. Chem. Soc.* 136 (2014) 9280–9283.
- [6] C. Dinh, H. Yen, F. Kleitz, T. Do, *Angew. Chem. Int. Ed.* 53 (2014) 6618–6623.
- [7] S. Ullah, E.P. Ferreira-Neto, A.A. Pasa, C.C.J. Alcântara, J.J.S. Acuña, S.A. Bilmes, M.L.M. Ricci, R. Landers, T.Z. Fermíno, U.P. Rodrigues-Filho, *Appl. Catal. B* 179 (2015) 333–343.
- [8] X. Weng, Q. Zeng, Y. Zhang, F. Dong, Z. Wu, *ACS Sustain. Chem. Eng.* 4 (2016) 4314–4320.
- [9] N. Liu, V. Haublein, X. Zhou, U. Venkatesan, M. Hartmann, M. Mackovic, T. Nakajima, E. Speicker, A. Osvet, L. Frey, P. Schmuki, *Nano Lett.* 15 (2015) 6815–6820.
- [10] W. Zhou, H. Fu, *ChemCatChem* 5 (2013) 885–894.
- [11] W. Qian, P.A. Greaney, S. Fowler, S. Chiu, A.M. Goforth, J. Jiao, *ACS Sustain. Chem. Eng.* 2 (2014) 1802–1810.
- [12] Y. Yuan, Z. Ye, H. Lu, B. Hu, Y. Li, D. Chen, J. Zhong, Z. Yu, Z. Zou, *ACS Catal.* 6 (2016) 532–541.
- [13] S. Ardo, G.J. Meyer, *Chem. Soc. Rev.* 38 (2009) 115–164.
- [14] R. Asahi, T. Morikawa, T. Ohwaki, K. Aoki, Y. Taga, *Science* 293 (2001) 269–271.
- [15] N. Shi, X. Li, T. Fan, H. Zhou, J. Ding, D. Zhang, H. Zhu, *Energy Environ. Sci.* 4 (2011) 172–180.
- [16] C. Han, M. Pelaez, V. Likodimos, A.G. Kontos, P. Falaras, K. O'Shea, D.D. Dionysiou, *Appl. Catal. B* 107 (2011) 77–87.
- [17] Y. Yu, Y. Tang, J. Yuan, Q. Wu, W. Zheng, Y. Cao, *J. Phys. Chem. C* 118 (2014) 13545–13551.
- [18] Y. Zhang, Q. Fu, Q. Xu, X. Yan, R. Zhang, Z. Guo, F. Du, Y. Wei, D. Zhang, G. Chen, *Nanoscale* 7 (2015) 12215–12224.
- [19] Y. Lin, H. Hsueh, C. Chang, H. Chu, *Appl. Catal. B* 199 (2016) 1–10.
- [20] R. Venkatkarthick, D.J. Davidson, S. Vasudevan, G. Sozhan, S. Ravichandran, *ChemistrySelect* 2 (2017) 288–294.
- [21] Y. Zhang, Z. Zhao, J. Chen, L. Cheng, J. Chang, W. Sheng, C. Hu, S. Cao, *Appl. Catal. B* 165 (2015) 715–722.
- [22] E.M. Samsudin, S.B.A. Hamid, J.C. Juan, W.J. Basirun, G. Centi, *Chem. Eng. J.* 280 (2015) 330–343.
- [23] D. Li, J. Jia, T. Zheng, X. Cheng, X. Yu, *Appl. Catal. B* 188 (2016) 259–271.
- [24] A. Meng, J. Zhang, D. Xu, B. Cheng, J. Yu, *Appl. Catal. B* 198 (2016) 286–294.
- [25] H. Li, J. Shang, Z. Ai, L. Zhang, *J. Am. Chem. Soc.* 137 (2015) 6393–6399.
- [26] X. Liu, G. Dong, S. Li, G. Lu, Y. Bi, *J. Am. Chem. Soc.* 138 (2016) 2917–2920.
- [27] C. Peng, X. Yang, Y. Li, H. Yu, H. Wang, F. Peng, *ACS Appl. Mater. Interfaces* 8 (2016) 6051–6060.
- [28] L. Liu, Y. Jiang, H. Zhao, J. Chen, J. Cheng, K. Yang, Y. Li, *ACS Catal.* 6 (2016) 1097–1108.
- [29] H. Zhang, Z. Xing, Y. Zhang, Z. Li, X. Wu, C. Liu, Q. Zhu, W. Zhou, *RSC Adv.* 5 (2015) 107150–107157.
- [30] X. Chen, L. Liu, F. Huang, *Chem. Soc. Rev.* 44 (2015) 1861–1885.
- [31] J. Dong, J. Han, Y. Liu, A. Nakajima, S. Matsushita, S. Wei, W. Gao, *ACS Appl. Mater. Interfaces* 6 (2014) 1385–1388.
- [32] H. Qin, Y. Bian, Y. Zhang, L. Liu, Z. Bian, *Chin. J. Chem.* 35 (2017) 203–208.
- [33] Y. Li, Y. Bian, H. Qin, Y. Zhang, Z. Bian, *Appl. Catal. B* 206 (2017) 293–299.
- [34] C. Tang, L. Liu, Y. Li, Z. Bian, *Appl. Catal. B* 201 (2017) 41–47.
- [35] Z. Bian, J. Zhu, H. Li, *J. Photochem. Photobiol. C* 28 (2016) 72–86.
- [36] F. Cao, Y. Li, C. Tang, X. Qian, Z. Bian, *Res. Chem. Intermed.* 42 (2016) 5975–5981.
- [37] X. Liu, G. Dong, S. Li, G. Lu, Y. Bi, *J. Am. Chem. Soc.* 138 (2016) 2917–2920.
- [38] L. Liu, Y. Jiang, H. Zhao, J. Chen, J. Cheng, K. Yang, Y. Li, *ACS Catal.* 6 (2016) 1097–1108.
- [39] Z. Xing, W. Zhou, F. Du, L. Zhang, Z. Li, H. Zhang, W. Li, *ACS Appl. Mater. Interfaces* 6 (2014) 16653–16660.
- [40] Z. Xing, H. Zhang, Z. Li, X. Zhang, Y. Zhang, L. Li, W. Zhou, *ChemPlusChem* 80 (2014) 623–629.
- [41] G. Zhang, Y. Zhang, M. Nadagouda, C. Han, K. O'Shea, S.M. El-Sheikh, A.A. Ismail, D.D. Dionysiou, *Appl. Catal. B* 07 (2013) 058.
- [42] K. Zhang, W. Zhou, L. Chi, X. Zhang, W. Hu, B. Jiang, K. Pan, G. Tian, Z. Jiang, *ChemSusChem* 9 (2016) 2841–2848.
- [43] J. Huo, Y. Hu, H. Jiang, C. Li, *Nanoscale* 6 (2014) 9078–9084.
- [44] W. Zhou, F. Sun, K. Pan, G. Tian, B. Jiang, Z. Ren, C. Tian, H. Fu, *Adv. Funct. Mater.* 21 (2011) 1922–1930.
- [45] X. Chen, L. Liu, P.Y. Yu, S.S. Mao, *Science* 331 (2011) 746–750.
- [46] X. Liu, Z. Xing, H. Zhang, W. Wang, Y. Zhang, Z. Li, X. Wu, X. Yu, W. Zhou, *ChemSusChem* 9 (2016) 1118–1124.
- [47] D. Li, Z. Xing, X. Yu, X. Cheng, *Electrochim. Acta* 170 (2015) 182–190.
- [48] J. Mao, L. Ye, K. Li, X. Zhang, J. Liu, T. Peng, L. Zan, *Appl. Catal. B* 144 (2014) 855–862.
- [49] J. Xu, F. Teng, C. Xu, Y. Yang, L. Yang, Y. Kan, *J. Phys. Chem. C* 119 (2015) 13011–13020.
- [50] J. Yu, J. Low, W. Xiao, P. Zhou, M. Jaroniec, *J. Am. Chem. Soc.* 136 (2014) 8839–8842.

- [51] J. Eom, S. Lim, S. Lee, W. Ryu, H. Kwon, *J. Mater. Chem. A* 3 (2015) 11183–11188.
- [52] V. Kiran, S. Sampath, *ACS Appl. Mater. Interfaces* 4 (2012) 3818–3828.
- [53] Y. Lin, C. Weng, Y. Lin, C. Shieh, F. Chen, *Sep. Purif. Technol.* 116 (2013) 114–123.
- [54] X. Yu, L. Wang, J. Zhang, W. Guo, Z. Zhao, Y. Qin, X. Mou, A. Li, H. Liu, *J. Mater. Chem. A* 3 (2015) 19129–19136.
- [55] W. Qian, P.A. Greaney, S. Fowler, S. Chiu, A.M. Goforth, J. Jiao, *ACS Sustain. Chem. Eng.* 2 (2014) 1802–1810.
- [56] Y. Fan, D. Han, B. Cai, W. Ma, M. Javed, S. Gan, T. Wu, M. Siddiq, X. Dong, L. Niua, *J. Mater. Chem. A* 2 (2014) 13565–13570.
- [57] S. Pany, K.M. Parida, *Phys. Chem. Chem. Phys.* 17 (2015) 8070–8077.
- [58] L. Kong, Z. Jiang, C. Wang, F. Wan, Y. Li, L. Wu, J. Zhi, X. Zhang, S. Chen, Y. Liu, *ACS Appl. Mater. Interfaces* 7 (2015) 7752–7758.
- [59] F. Zuo, L. Wang, T. Wu, Z. Zhang, D. Borchardt, P. Feng, *J. Am. Chem. Soc.* 132 (2010) 11856–11857.